

Transmission surface plasmon resonance microscopy

Olivier Loison and Emmanuel Fort

Citation: [Applied Physics Letters](#) **103**, 133110 (2013); doi: 10.1063/1.4822431

View online: <http://dx.doi.org/10.1063/1.4822431>

View Table of Contents: <http://scitation.aip.org/content/aip/journal/apl/103/13?ver=pdfcov>

Published by the [AIP Publishing](#)

An advertisement for Integrated Engineering Software. It features a yellow background with a blue and green abstract graphic on the right. The text 'INTEGRATED ENGINEERING SOFTWARE' is in a bold, blue, sans-serif font. Below it, 'Particle and Beam Ray Tracing Simulation' is in a smaller, grey, sans-serif font, followed by 'Send us your model and see LORENTZ in action'. A 'LEARN MORE' button is in a white, sans-serif font with a shadow effect.

INTEGRATED
ENGINEERING SOFTWARE

Particle and Beam Ray Tracing Simulation
Send us your model and see LORENTZ in action

LEARN MORE

Transmission surface plasmon resonance microscopy

Olivier Loison and Emmanuel Fort^{a)}

Institut Langevin, Ecole Supérieure de Physique et de Chimie Industrielles (ESPCI) ParisTech, CNRS UMR 7587, 1 rue Jussieu, 7528 Paris Cedex 05, France

(Received 31 May 2013; accepted 11 September 2013; published online 26 September 2013)

We present a microscopy technique to image minute variations of optical properties at the interface of a metallic thin-film. This technique is based on an original transmission configuration of surface plasmon resonance sensors. It combines high diffraction-limited lateral resolution with unaltered refractive index sensitivity. Transmitted light is obtained by using near-field transducers positioned at the metal/dielectric interface to probe the propagative surface plasmon dispersion curve. This label-free technique can find applications in highly multiplexed molecular sensing or full-field surface microscopy. As an example, we show tomography images of silica nanometric patterns.
 © 2013 AIP Publishing LLC. [<http://dx.doi.org/10.1063/1.4822431>]

Surface Plasmon Resonance (SPR) sensors enable the measurement of minute variations of optical properties near a metallic interface. SPR principle relies on the measurement of changes in the propagating surface plasmon (PSP) dispersion curve. These modifications are induced by the refractive index changes of the dielectric medium near the interface.¹ In SPR sensors, the variations of the refractive index are related to the surface concentration of detected molecules.² SPR technique is widespread in biosensing applications. In particular, it provides a way to monitor the dynamical interactions between biomolecules of interest (analytes) and ligands bound to the surface of the resonator-chip.³ Commercial sensors have a typical sensitivity of 1 pg/mm², corresponding to 10⁻⁷ Relative Index Unit (RIU).⁴ In the standard configuration, SPR sensors are composed of a thin metallic layer separating the medium of interest with a refractive index n_d from a glass slide with a refractive index n_g placed on an prism. The PSP propagating at the medium of interest/metallic interface is excited, through the prism, from the side with a higher refractive index ($n_g > n_d$) to enable momentum matching (Kretschmann configuration). The resonance conditions give the following relation for the incident angle θ_{SPR} :

$$n_g \sin \theta_{SPR} = \sqrt{\frac{\epsilon_m \epsilon_d}{\epsilon_m + \epsilon_d}}, \quad (1)$$

where ϵ_m and $\epsilon_d = n_d^2$ are the permittivity of the metal and of the medium of interest, respectively. The angle θ_{SPR} is thus sensitive to the local refractive index of the dielectric medium. The presence of an extinction peak in the reflected light acquired as a function of the incidence angle is directly related to the PSP dispersion curve and the PSP excitation.

More recently, standard SPR configurations have been modified to enable multiplexing for high throughput sensing⁵ and cell imaging applications.⁶ The sensor chip is imaged on a camera using an additional lens. However, because of the presence of the prism, the numerical aperture (NA) of the added lens is limited (typically to 0.2 NA), resulting in a poor lateral resolution of the image ($\sim 3 \mu\text{m}$).⁷ Alternatively,

a prism-less configuration using an immersion oil high NA objective lens has been proposed.^{8,12,13} In that case, the highest diffraction limited resolutions become accessible. However, the refractive index sensitivity is dramatically reduced by unavoidable poorly controlled incidence beam (spatial heterogeneity and angular uncertainty) and angular projection effects of the excitation beam within the objective. Sensitivity can only be partially recovered when using scanning configurations.⁸⁻¹¹

Here, we present an original transmission configuration that enables the combination of the highest diffraction limited lateral resolutions whilst maintaining the refractive index sensitivity of standard SPR. This configuration designated by transmission SPR (tSPR) enables the joint use of a prism for its unmatched ability to control the excitation beam together with a high numerical aperture objective which can freely access to the interface from the sample side. High lateral resolution is thus simultaneously obtained in a full-field configuration.

Figure 1(a) shows the theoretical reflectance curve (solid lines) as a function of the excitation angle. These curves are signatures of the dispersion curves of the PSP at the dielectric medium/metal interface. They present a sharp extinction for a specific angle θ_{SPR} associated to the PSP excitation. θ_{SPR} shifts to higher angles as the refractive index of the dielectric medium n_d increases (black and bright curves, respectively). Standard SPR measures this shift to deduce the changes in the refractive index of the dielectric medium at the interface. In the case of biosensors, it is ultimately related to the surface concentration of interacting analytes.⁷ PSP excitation is associated to the presence of an EM field (polariton) at the dielectric medium/metal interface. This field is evanescent, decaying exponentially in the dielectric medium.¹⁴ The dashed line in Fig. 1(a) shows the normalized EM intensity at the interface as a function of the incidence angle. The observed peak is a direct signature of the PSP excitation and mirrors the sharp extinction in the reflectance curve. Similarly, it also shifts to higher angles as the refractive index of the dielectric medium increases (dark and bright curves, respectively).

Although this field is evanescent, it can be detected in the far-field by the presence of small fluorescent or scattering

^{a)}Electronic mail: emmanuel.fort@espci.fr

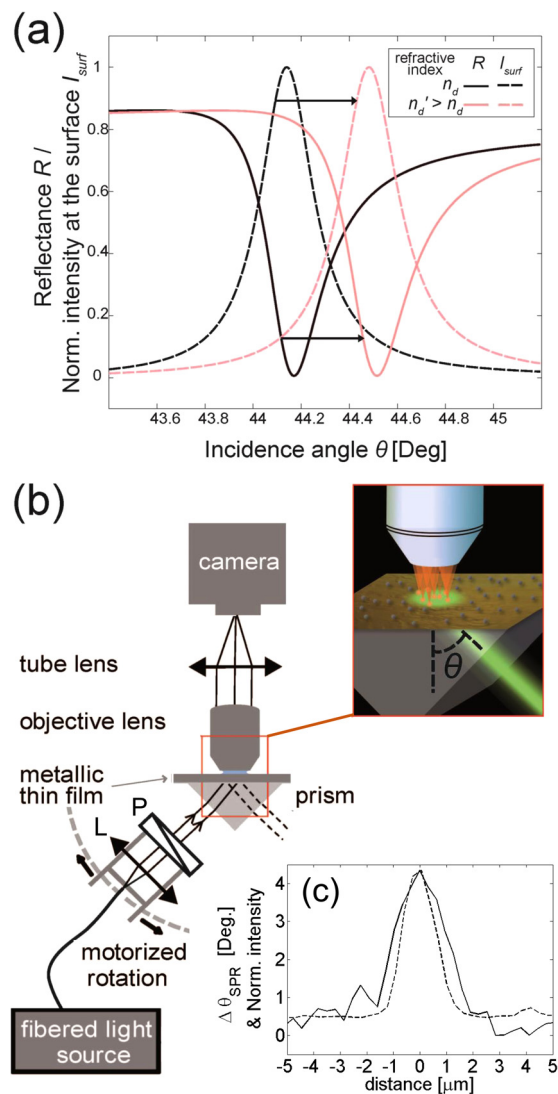


FIG. 1. (a) tSPR principle: in the standard SPR configuration, the normalized reflectance curves vs. the incidence angle (solid lines) shift as the refractive index of the dielectric medium is increased from $n_d = 1.024$ (black) to $n'_d = 1.030$ (bright red). In SPR, the signal is proportional to the light intensity at the dielectric medium/metal interface (dashed lines), which also shifts as the refractive index of the dielectric medium is increased. These curves are obtained using the Fresnel theory at $\lambda = 635$ nm for a multi-layer: glass/2 nm chromium/54 nm silver/dielectric medium. (b) Experimental setup for tSPR microscopy: a standard upright microscope is equipped with a standard Kretschmann configuration setup for sample illumination. The light source is a fibered LED mounted on a computer-controlled motorized rotation stage. The beam is collimated with the lens (L) and p-polarized (P). The sample comprises fluorescent or scattering emitters placed at the dielectric medium/metal interface (inset). The sensor surface is imaged on a CCD camera using a water immersion objective lens. (c) Profiles of the SPR angle shift $\Delta\theta_{SPR}$ (solid line) and of the normalized scattered intensity (dashed line) obtained from the tSPR angular scan of a nanometric object.

transducers situated near the interface. This method has been used to detect surface-plasmon propagation by photoinduced scattering using a focused probe laser beam.¹⁵ For a large range of light intensity (far from the saturation regime), their emission is directly proportional to the local light intensity. Hence, the transmitted emission is proportional to the intensity at the interface (see Fig. 1(a)). The transducers thus act as local near-field probes of the PSP excitation. Moreover, the evanescent field at the interface can be amplified on resonance as compared with the incident field.¹⁶ This leads to a high signal to noise ratio even for low transduction yields.

Note that this property together with the confinement of the field at the interface has been used in enhanced fluorescence sensing¹⁷ and imaging.¹⁸ These techniques however are based on a very different principle as compared with tSPR. The detected light is proportional to the surface concentration of detected molecules, the PSP sensitivity to optical changes plays no role, and the molecules of interest need fluorescence tagging.

Because of their similar signal to noise ratio and angular dependence, standard SPR and tSPR have similar sensitivities. Fluorescent or scattering emitters locally probe the PSP excitation through their associated evanescent EM field. The desired concentration of transducers induces only very small modifications in the dispersion relation of the PSP. In any case, these changes can be taken into account in the calibration process. It is important that the transduction yield remains constant during the entire measurement. For this reason, care must be taken concerning possible photobleaching when using fluorescent probes. Similarly, the sample should remain still during the time of acquisition to avoid fluorescence or scattering fluctuations.

Figure 1(b) shows the experimental setup for the tSPR configuration. It consists of a standard prism-based SPR excitation setup combined with an upright microscope equipped with a CCD camera. The sample is mounted on a triangular prism made of N-SF11 glass ($n_p(\lambda = 532 \text{ nm}) = 1.795$ and $n_p(\lambda = 640 \text{ nm}) = 1.778$). The excitation light is collimated through the prism on the sensor chip. This latter is composed of a thin continuous metallic layer of gold ($n_m(\lambda = 640 \text{ nm}) = 0.172 + 3.50i$) or silver ($n_m(\lambda = 532 \text{ nm}) = 0.054 + 3.43i$ and $n_m(\lambda = 640 \text{ nm}) = 0.056 + 4.30i$)¹⁹ of typically 50 nm to maximize the PSP excitation.¹ The thin film has been obtained by e-beam evaporation on a glass slide ($n_g = 1.515$) after deposition of an adhesion layer of 2 nm of chromium. An index-matching liquid (immersion oil) insures continuity between the prism and the glass slide. The light source can be either a continuous laser ($\lambda = 640 \text{ nm}$) or a LED emitting in the green (centered at $\lambda = 532 \text{ nm}$) or in the red (centered at $\lambda = 635 \text{ nm}$). The source is coupled to an optical fiber mounted on a motorized rotation stage. The fiber output beam is collimated by lens (L) and p-polarized by a polarizer (P) to excite the PSP. A LabVIEW program synchronizes the camera with the rotation stage for angular scanning. This angular interrogation allows one to fit the resonance peak of the PSP. It is therefore possible to monitor the spatial or temporal variations of the refractive index in the vicinity of the interface. The peak maximum is obtained from a gaussian fit, and the associated refractive index is deduced using a standard multi-layer Fresnel model.

The lateral resolution of the tSPR technique can be obtained by inducing a point variation of the refractive index and measuring the width of the SPR angle variation on the image. Figure 1(c) shows the profile (solid line) of the SPR angle shift $\Delta\theta_{SPR}$ induced by a nanometric object (smaller than the diffraction limit). The intensity profile associated with the point spread function of the microscope is also shown for comparison (dashed line). The FWHM of the SPR and intensity profiles are similar, $2.4 \pm 0.2 \mu\text{m}$ and $1.4 \pm 0.1 \mu\text{m}$, respectively. Hence, the lateral resolution of the tSPR image is slightly larger than the diffraction limit of the microscope.

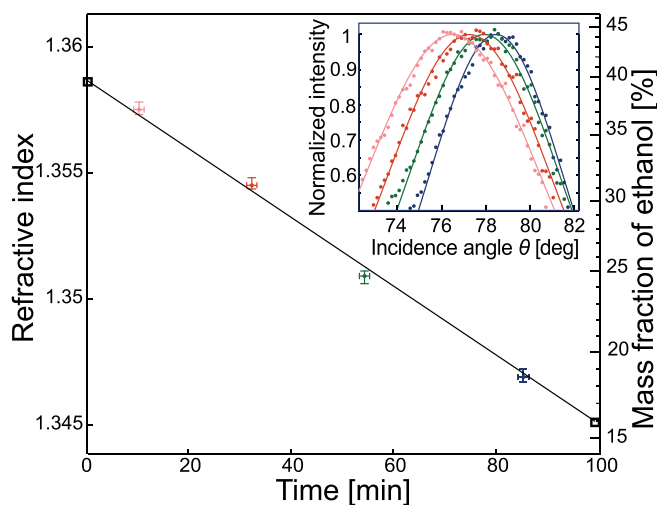


FIG. 2. Refractive index variations and associated changes of ethanol mass fraction as a function of time during the evaporation of a water-ethanol mixture. A low concentration of Rhodamin 700 has been added to the mixture to probe the EM field associated to the PSP. The dots are obtained by fitting the fluorescence signal vs incidence angle with a gaussian fit (see inset) and using a multi-layer Fresnel model. The multi-layer consists of glass/2 nm chromium/50 nm gold/a monolayer of dodecanethiol/ethanol-water mixture. The squares represent refractive index measurements obtained with a refractometer. The right axis is deduced using refractive index data for ethanol-water mixture of Ref. 20.

We first validate the tSPR method by performing measurements on refractive index changes of the entire dielectric medium. This enables us to measure the sensitivity of the technique directly in RIU.⁷ We measured the changes of refractive index during the evaporation process of a water/ethanol mixture. A protective layer of dodecanethiol has been deposited on the resonator-chip prior to the experiment. The tSPR signal is produced by a low concentration of fluorescent dyes (Rhodamin 700) that have been dispersed in the solution. These near-field transducers are homogeneously distributed in the dielectric medium and are continuously renewed near the interface insuring a constant signal transduction yield. Figure 2 shows the decrease of the refractive index versus time as the concentration of the mixture changes due to evaporation. The inset image shows the normalized fluorescence intensity as a function of the incidence angle at various times associated with the experimental plots in Figure 2. The curves represent gaussian fits to obtain the

angular position of the maxima. The two refractive indices at time zero and after 100 min (squares) have been obtained with a refractometer. The refractive index of the medium decreases from 1.359 to 1.345 due to the preferential evaporation of the ethanol. From the measured refractive index (left axis) it is possible to deduce the percentage of ethanol in the mixture (right axis) using the data in Ref. 17. The precision of the relative refractive index measurements is about 10^{-4} RIU. This sensitivity is limited by the thermal fluctuations of the setup with typical temperature variations of the order of 1°C . Note that in standard SPR devices, a temperature control down to the millidegree Celsius improves their sensitivity by about 3 orders of magnitude.⁷ Increasing the sensitivity of our set-up would similarly require the use of a fine thermostated environment.

We now focus on the imaging performance of tSPR microscopy to map the local variations of optical properties near the interface. The samples are composed of silica patterns deposited on the resonator chip. Silica thickness takes two values: 15 nm or 18 nm. Figure 3(a) shows a typical 3D surface tomography obtained from the tSPR measurements using a multi-layer Fresnel model with a refractive index for silica $n_{\text{SiO}_2} = 1.46$. Figure 3(b) shows a close-up of a 3-nm-thick step obtained in water and in air. The associated averaged profiles integrated on the $30\ \mu\text{m}$ width of these areas are shown in Figure 3(c). The tomography mapping is very similar in the two cases. The two measurements in water and in air give a 3 nm thickness in agreement with the measured thickness during a deposition process (within 10% accuracy). The slightly larger value in the case of water immersion can possibly be explained because of neglecting a slight increase of the silica-layer refractive index induced by silica porosity. In water, the signal to noise ratio S/N is reduced by one order of magnitude as compared to measurements in water ($S/N_{\text{water}} \approx 30$ and $S/N_{\text{air}} \approx 300$). This is a direct consequence of the much smaller difference between silica/water refractive indices than the silica/air ones.

Image resolution in tSPR is limited by the NA of the objective lens that can be as high as the refractive index of the dielectric medium. However, the sensitivity to the local refractive index in the PSP propagation direction is convolved by the PSP propagation along the interface. This length depends on the dissipation processes involved. A first process is the absorption in the metal through the imaginary

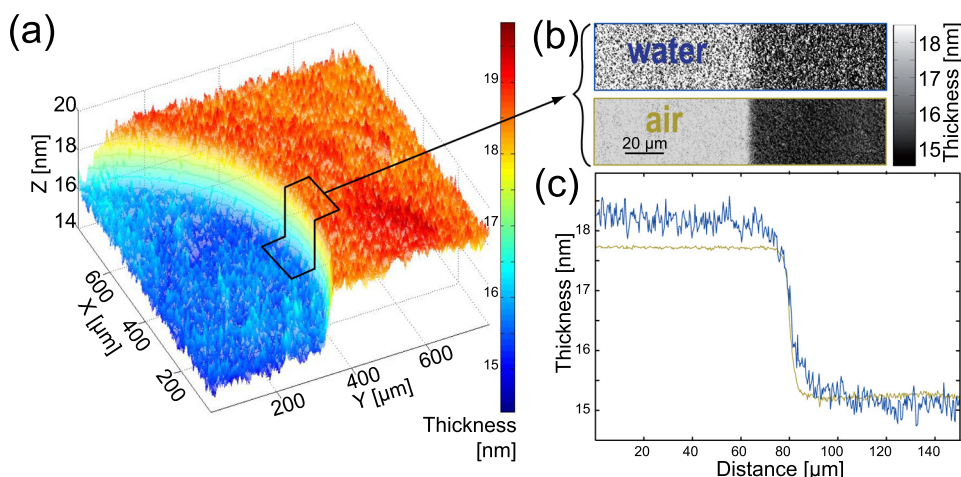


FIG. 3. (a) 3D tomography of a silica pattern deposited on the metallic sensor chip by lithography obtained from tSPR microscopy using a multi-layer Fresnel model. The tSPR signal is produced by scattering on the intrinsic roughness of the metallic layer. Illumination is provided by a red LED source with a wavelength center at 635 nm. (b) Close up of the highlighted area in (a) showing a detail of the tomography image for the 3 nm step of silica obtained in water and in air. (c) Averaged profiles of the silica step obtained from (b) in water and in air.

part of its refractive index. This depends strongly on the nature of the metal and on the light wavelength.¹⁴ Second, damping processes induced by the film roughness can also cause a reduction in the PSP propagation length.²¹ Roughness induces scattering into other surface plasmon states and into the dielectric medium. Note that this process is being used to provide natural *in situ* near-field transducers for the tSPR signal in the present case. However, the small roughness involved here makes this effect negligible to change the PSP propagation length.²² A third process is the coupling into leakage radiation modes in the glass medium. This radiative emission process, called inverse Kretschmann effect, depends strongly on the film thickness.²³ As the thickness of the metal layer is decreased, the coupling efficiency is increased, and radiation loss dominates the wave attenuation. Hence, the thickness of the metallic thin film permits tuning the propagation length down to the micrometer.²⁴ To show the role of the propagation length, we have chosen a 54 nm thick silver metallic thin film for which absorption is small resulting in a measurable propagation length larger than the diffraction limited resolution.

Figure 4(a) shows the normalized topography map of a 3 nm silica step obtained from tSPR images for PSP propagation orthogonal and parallel to the step at different wavelengths (532 nm and 635 nm). The deduced averaged normalized profiles are plotted in Figure 4(b). These profiles are obtained by integrating the topography signal on a width of 30 μm . The effect of the wavelength and the PSP propagation direction are clearly visible. To characterize it, we use the distance d separating signals associated with 10% and 90% of the step amplitude. The profile obtained with a parallel direction is the steepest $d^{\parallel} = 4 \mu\text{m}$. This profile is identical for an excitation wavelength in the red or in the green. Conversely the step profile changes significantly with the excitation wavelength for an orthogonal PSP propagation: $d_g^{\perp} = 11 \mu\text{m}$ for excitation in the green and $d_r^{\perp} = 24 \mu\text{m}$ for excitation in the red. For a PSP propagation parallel to the step, the tomography resolution is

limited by diffraction associated to the NA of the objective lens. The lateral resolution is usually defined by $\delta \approx 0.5\lambda/\text{NA}$. In the present case, the objective NA is equal to 0.8; hence, δ is smaller than one micron in the entire visible spectrum. This is much smaller than the characteristic length of the step profile resulting from the silica deposition process. Conversely, for the orthogonal profiles, the characteristic length of the step profile must be compared to the propagation length of the PSP. Using the expression given in Refs. 22 and 23 that takes into account the absorption in the metallic thin film and the radiative emission by the inverse Kretschmann process, we obtain for the propagation length of PSP, $L_g = 18 \mu\text{m}$ and $L_r = 43 \mu\text{m}$, respectively, in the green and red spectral region (the refractive indices of the silver being $n_{\text{Ag}}(\lambda/532 \text{ nm}) = 0.054 + 3.429i$ and $n_{\text{Ag}}(\lambda/635 \text{ nm}) = 0.056 + 4.293i$, from Ref. 19). The relative values of these lengths are in good agreement with the measured step profiles ($L_r/L_g = 2.4$ and $d_r^{\perp}/d_g^{\perp} = 2.2$). The propagation length is very sensitive to the illumination wavelength as a result of the high spectral variations of the imaginary part of the refractive index of the metal. It is a general feature that the propagation length increases in the red as damping decreases in metals.

In the present case, the radiation losses to leaky modes are the dominant damping process. For thick silver samples, propagation lengths of $L_g = 28 \mu\text{m}$ and $L_r = 66 \mu\text{m}$ would have been obtained. Note that the PSP propagation length can be reduced down to the diffraction limited resolution by a proper choice of metal and thin film thicknesses (for instance with a 40 nm thick gold film). In that case, tSPR technique would reach a typical resolution of less than a micron (with NA up to n_d), conversely to standard SPR geometries limited by the geometry of the setup (with typically $\text{NA} = 0.2$). Without loss of sensitivity, tSPR enables a gain of more than one order of magnitude in biosensors density and open new perspectives in surface imaging. In particular, tSPR can combine resolution and sensitivity needed for a label-free imaging of membrane and adhesion processes of living cell.

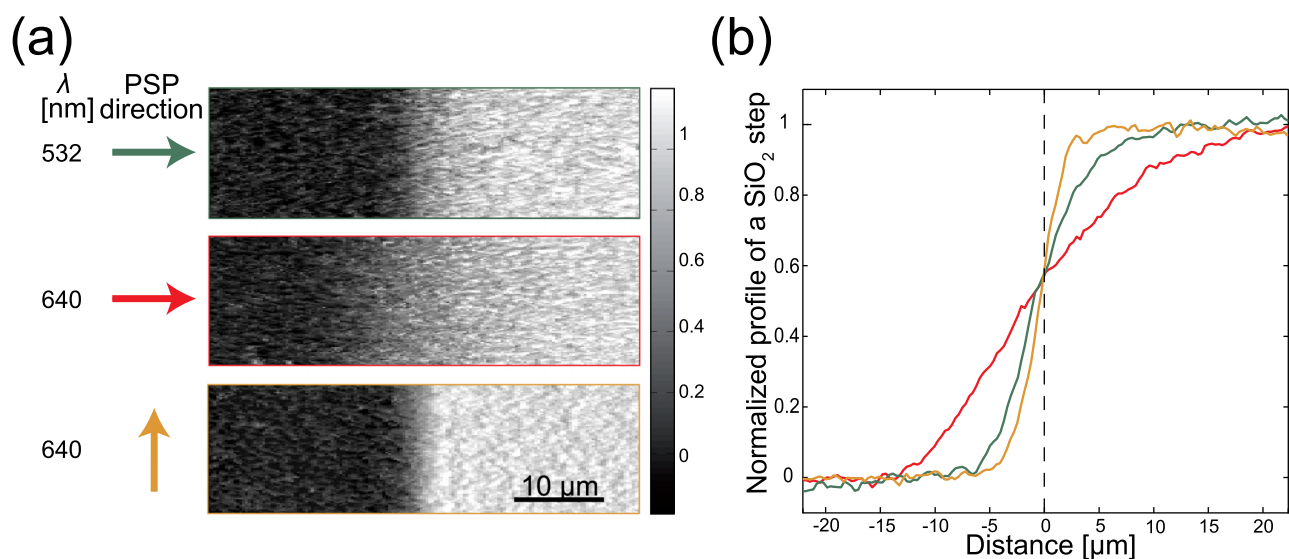


FIG. 4. Normalized topography of a 3 nm step of silica obtained from tSPR images for PSP propagation parallel and orthogonal to the step and for green (532 nm) and red (635 nm) illumination wavelengths. (c) Normalized topography profiles of the same step obtained from the areas shown in (a) by averaging over the 30 μm width. The dashed black line represents the position of an ideal step.

We would like to thank X. H. Vu, T. Barroca, C. Boccara, P. Bon, K. Balaa, S. Grésillon, and S. Lèveque-Fort for fruitful discussions, F. Monti for his valuable advices and the access to the cleanroom, and F. Quinlan-Pluck for helpful comments on this letter. We acknowledge the financial support of the AXA Research Fund, the French National Research Agency, and French Program “Investments for the Future” (LABEX WIFI).

¹H. Raether, *Surface Plasmons on Smooth and Rough Surfaces and on Gratings* (Springer, Berlin, Germany, 1988).

²J. Homola, *Surface Plasmon Resonance Based Sensors*, edited by J. Homola (Springer, Berlin, Germany, 2006).

³J. M. McDonnell, *Curr. Opin. Chem. Biol.* **5**, 572 (2001).

⁴Y. H. Huang, H. P. Ho, S. Y. Wu, and S. K. Kong, *Adv. Opt. Technol.* **2012**, 471957.

⁵N. Bassil, E. Maillart, M. Canva, Y. Lvy, M.-C. Millot, S. Pissard, R. Narwa, and M. Goossens, *Sens. Actuators B* **94**, 313 (2003).

⁶K.-F. Giebel, C. Bechinger, S. Herminghaus, M. Riedel, P. Leiderer, U. Weiland, and M. Bastmeyer, *Biophys. J.* **76**, 509 (1999).

⁷E. Fort, in *Plasmonics in Optics in Instruments: Applications in Biology and Medicine*, edited by J.-P. Goure (John Wiley & Sons, Inc., Hoboken, USA, 2013), pp. 179–216.

⁸M. G. Somekh, S. G. Liu, T. S. Velinov, and C. W. See, *Opt. Lett.* **25**, 823 (2000).

⁹L. Berguiga, T. Roland, K. Monier, J. Elezgaray, and F. Argoul, *Opt. Express* **19**, 6571 (2011).

¹⁰M. M. A. Jamil, M. C. T. Denyer, M. Youseffi, S. Britland, S. Liu, C. See, M. Somekh, and J. Zhang, *J. Struct. Biol.* **164**, 75 (2008).

¹¹A. N. Naimushin, S. D. Soelberg, D. K. Nguyen, L. Dunlap, D. Bartholomew, J. Elkind, J. Melendez, and C. E. Furlong, *Biosens. Bioelectron.* **17**, 573 (2002).

¹²K. Moh, X.-C. Yuan, J. Bu, S. W. Zhu, and B. Z. Gao, *Opt. Express* **16**, 20734 (2008).

¹³B. Huang, F. Yu, and R. Zare, *Anal. Chem.* **79**, 2979 (2007).

¹⁴W. L. Barnes, A. Dereux, and T. W. Ebbesen, *Nature* **424**, 824 (2003).

¹⁵T. Velinov, M. G. Somekh, and S. Liu, *Appl. Phys. Lett.* **75**, 3908 (1999).

¹⁶E. Fort and S. Grésillon, *J. Phys. D: Appl. Phys.* **41**, 013001 (2008).

¹⁷T. Liebermann and W. Knoll, *Colloids Surf.* **171**, 115 (2000).

¹⁸R.-Y. He, G.-L. Chang, H.-L. Wu, C.-H. Lin, K.-C. Chiu, Y.-D. Su, and S.-J. Chen, *Opt. Express* **14**, 9307 (2006).

¹⁹P. B. Johnson and R. W. Christy, *Phys. Rev. B* **6**, 4370 (1972).

²⁰R. H. Pickard, A. H. J. Houssa, and H. Hunter, *International Critical Tables of Numerical Data, Physics, Chemistry and Technology*, 1st ed. (Knovel, Norwich, UK/New York, USA, 2003), p. 67.

²¹D. L. Mills and A. A. Maradudin, *Phys. Rev. B* **12**, 2943 (1975).

²²A. Bouhelier and G. P. Wiederrecht, *Opt. Lett.* **30**, 884 (2005).

²³E. Kretschmann, *Z. Phys.* **241**, 313 (1971).

²⁴A. Bouhelier and G. P. Wiederrecht, *Phys. Rev. B* **71**, 195406 (2005).